

Figure 1. Shown are the islands at toroidal position $\phi = 0$ (left) and $\phi = \pi/5 = 36^\circ$ (right) as dots as well as the target structures used in the simulations.

Parametrisation of target heat flux distribution and study of transport parameters for boundary modelling in W7-X

David Bold^a, Felix Reimold^a, Holger Niemann^a, Yu Gao^a, Marcin Jakubowski^a, Carsten Killer^a, Victoria R. Winters^a and the W7-X team^{a,b}

^aMax Planck Institute for Plasma Physics, Wendelsteinstr. 1, 17491 Greifswald, Germany

^bSee Klingner et al 2019 [1] for the W7-X Team

E-mail: dave@ipp.mpg.de

25 April 2022

Abstract. Modelling the scrape-off layer of a stellarator is challenging due to the complex magnetic 3D geometry. The here presented study analyses simulations of the scrape-off layer (SOL) of the stellarator Wendelstein 7-X (W7-X) using the EMC3-EIRENE code for the magnetic standard configuration. Comparing with experimental observations, the transport model is validated. Based on the experimentally observed strike line width, the anomalous transport coefficients, used as input to the code are determined to around $0.2 \text{ m}^2/\text{s}$. This is however in disagreement with upstream measurements, where such small cross-field transport leads to temperatures higher than measured experimentally.

1. Introduction

In order to operate fusion power plants based on the magnetic confinement concept the power flux on the plasma-facing surfaces needs to be controlled to prevent the overloading of the structures. Predictive modelling, necessary for design of next-step fusion devices, requires successful validation via comparison to existing experimental devices to ensure all important underlying physics is included in the code. One of these devices is Wendelstein 7-X (W7-X), an advanced stellarator with reduced neoclassical transport [2, 3, 4, 1, 5], which had its first divertor operational campaign in 2017 - 2018.

In contrast to tokamaks, the scrape-off layer (SOL) of W7-X is inherently three dimensional. W7-X features a 5-fold toroidal symmetry. Each of the 5 modules is in itself stellarator symmetric and can be split into two half modules. The SOL of W7-X features an island divertor, where in the standard configuration the 5 resonant islands are intersected by 10 divertor modules [6, 7, 8]. A plot of the islands and the intersection with the divertor is shown in fig. 1. The upper halves of the modules have even numbers, namely 18, 28, 38, 48, 58, and the lower half-modules have uneven numbers, 19 to 59. The half-modules $x8$ and $x9$ are in the x -th module. The divertors carry the numbers of the respective half-modules they are located within.

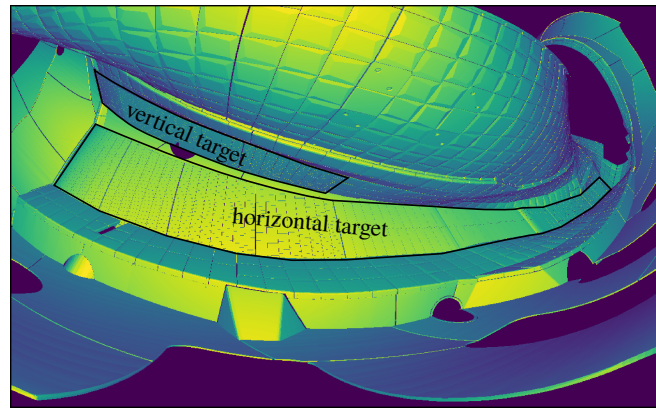


Figure 2. Synthetic view of the IR camera on the target.

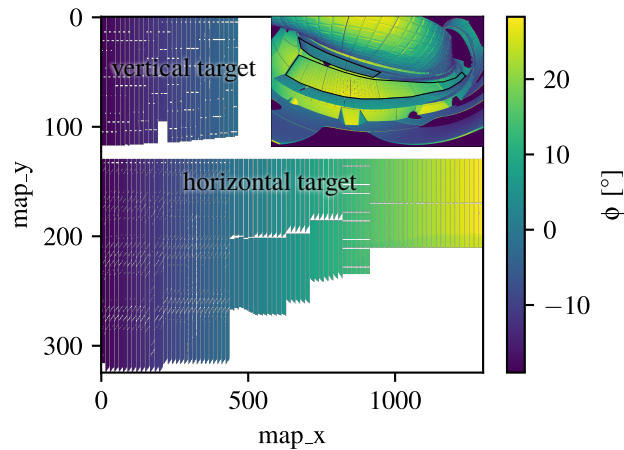


Figure 3. Mapped view of the target. The coordinates map_x and map_y are not directly related to physical quantities. map_x is roughly aligned with the magnetic field, while map_y is roughly orthogonal to the magnetic field. The pumping gap is around $\text{map}_y \approx 125$. The finger structures extend roughly 15 pixel in map_x direction. In the top right is an inset of fig. 2. The so called low iota target is on the horizontal target, for $\phi < 0$. Note that all targets are mapped to this ϕ coordinate. Upper divertors are mapped to negative toroidal angle, due to stellarator symmetry. Divertors are also shifted by $\frac{n-2\pi}{5}$ due to the 5 fold symmetry of W7-X.

The lack of toroidal symmetry makes connection and comparison of experimental measurements at different toroidal locations extremely complex. As such, there is great demand for 3D modelling, where synthetic diagnostics can be implemented to help understand whether differing diagnostic measurements are truly in disagreement or if differences are due purely to spatial variations in the plasma [9]. However, before such an analysis can be performed, it is critical to first validate the simulations, which itself requires diagnostic input covering as much of the SOL plasma domain as possible.

The anomalous cross-field transport in the SOL of fusion plasmas is often considered to be dominated by turbulence. In W7-X experiments, SOL turbulence and turbulent transport has been observed [10, 11, 12, 13]. As fully turbulent simulations of the full SOL are computationally extremely challenging, simpler models are generally used, such as fluid transport codes [14]. There the turbulence is effectively represented by anomalous diffusion coefficients.

This work validates the diffusion-based anomalous transport of EMC3-EIRENE in the absence of drifts in the model [15, 16] by using spatially constant transport coefficients. The simulation data is compared with experimental data from W7-X from the infra-red heat flux diagnostic and the reciprocating electric probes. This work extends previous work and especially addresses remaining discrepancies between simulations and experiments [16, 15, 17, 18, 19, 20, 21, 14]. The here presented analysis is restricted to the magnetic standard configuration.

The current paper is organized as follows: Section 2 the newly developed methods for comparing the heat-fluxes from experiments and simulations is presented. In section 3 the experimental data is presented, where the toroidal power distribution and the strike line width is seen. In the following section, the simulations are presented. Section 5 summarises and discusses the results, here it is seen that a spatially constant diffusion coefficient cannot simultaneously match downstream and upstream conditions in the selected magnetic configuration. The main conclusions are presented in the final section.

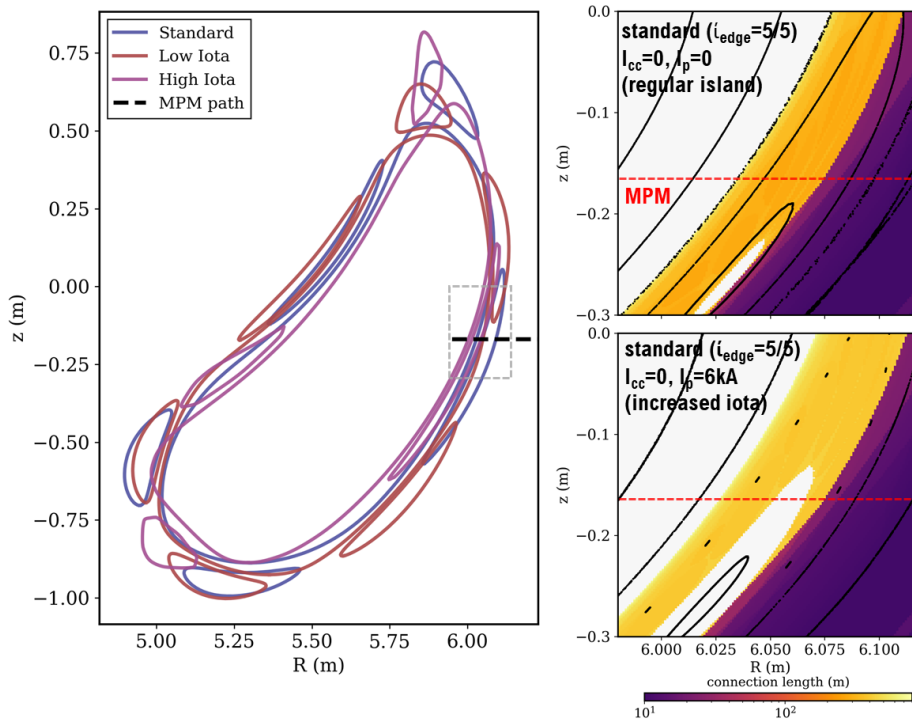


Figure 4. Position of the MPM diagnostic. Reproduced with kind permission from [25].

2. Method

2.1. W7-X diagnostics

In this work, two diagnostics are used for comparison to simulation data: one is measuring downstream at the divertor targets and the other upstream. Both downstream and upstream parameter comparisons are important to determine if the EMC3-EIRENE simulations successfully reproduce features across the entire SOL. The downstream measurement used is the infra-red (IR) camera system [22], which fully covered the area of the 10 divertors in the previous experimental campaign, with data available for 9 of the 10.

The temperature is derived from the IR radiation. The heat-flux is calculated by the evolution of the temperature profiles using the two-dimensional thermal model THEODOR [23]. This heat-flux is used to assess the validity of the employed SOL transport model in EMC3-EIRENE as the heat-flux has a high spatial resolution. The spatial resolution is around 3 mm the noise level is around 0.25 MW/m^2 .

The second diagnostic used for comparison is the multi-purpose manipulator (MPM). The MPM can be equipped with different probe heads to provide profiles of various plasma parameters such as T_e , n_e , poloidal mach number and more [24, 25].

In the here presented analysis, the MPM was equipped with Langmuir probes, that have been used to measure the electron density and temperature in the SOL of W7-X. This provides plasma parameters upstream and thus complements the downstream comparison provided by the heat-flux measurements at the divertor. Unlike the infra-red diagnostic the MPM is only present in one location, thus does not give a direct measurement of up-down asymmetries [8] or field errors [26]. The path of the MPM is shown in fig. 4.

2.2. Heat-Flux distribution analysis

The strike-line width and amplitude is used in order to make the heat-flux profiles more comparable between modelling and experiments. The IR data is mapped onto the image format as shown in fig. 3. The divertor is split into smaller structures, called fingers, that extend mostly in poloidal direction. 1D slices of the data are analysed, taking slices roughly perpendicular to the magnetic field lines, in the map_y direction from fig. 3. This gives around 15 1D slices for each finger. These 1D slices are then fitted to a function consisting of a constant background plus 2 Gaussian. The positions of the peaks are constrained to be within the data slice. The lower bounds for the peak is 3 times the grid spacing, to avoid fitting a single outlier, rather than the general shape of the data. For fitting the Trust Region Reflective algorithm (`trf`) from `scipy.optimize.least_squares` is used [27, 28].

In order to decrease the computational cost as well as to decrease the impact of noise, 10 time frames are averaged for fitting. This gives a time resolution of 100 ms. The study is restricted to steady-state profiles as the EMC3-EIRENE code only provides steady-state solutions. Although the evolution of the toroidal plasma current throughout the discharge may change the location and width of the strike line, the movement is on the order of mm/s and does not significantly impact the

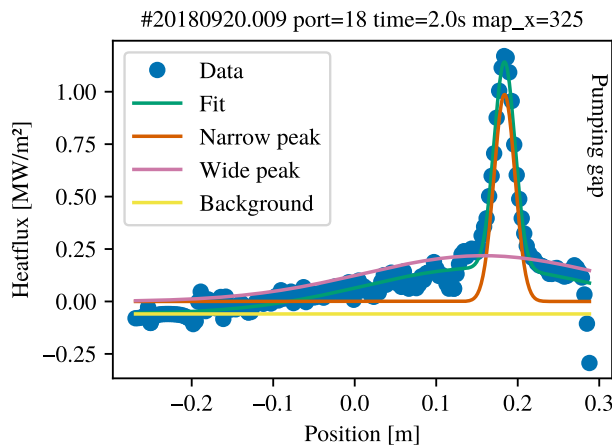


Figure 5. Plot of the IR data for the horizontal target at $\text{map}_x=325$. It can be seen that the data consists of a narrow, high in amplitude peak, as well as a broader feature with a significantly smaller amplitude. The fitted constant background is in this case negligible.

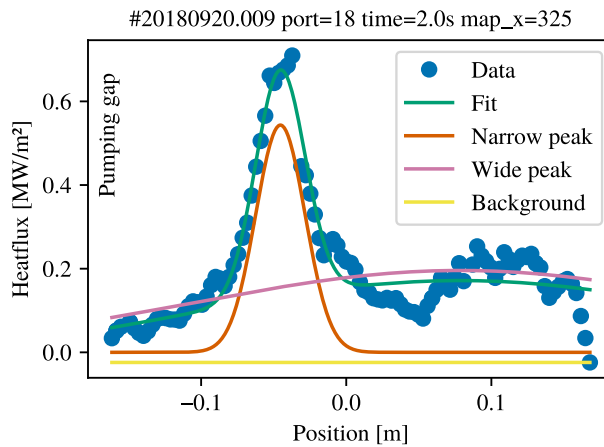


Figure 6. Plot of the IR data for the vertical target at $\text{map}_x=325$. The fit detects the strike line as “Narrow peak”. The “Wide peak” combined with the “Background” fit the background as well the reflections at 0.1 m.

result over a 100 ms time window [29].

For each averaged time slice, each pixel row of each finger is separately analysed. One should note, that for one map_x value there can be several data slices, as the horizontal target and the vertical target are different fingers but share the same map_x value. Similarly, in the middle of the horizontal target, between $450 \lesssim \text{map}_x \lesssim 800$ the data is split into two fingers, one close to the gap, and one further away. If the peak heat-flux is below the noise-level of 0.25 MW/m^2 , no fit is attempted.

Examples of the fitted data are shown in fig 5 and fig. 6 for the horizontal target and vertical target. Especially on the vertical target for $\text{map}_x \text{ less approx } 450$ the fit is generally good. On the middle of the horizontal target, especially for the fingers distant from the pumping gap, the heat-flux is very low, and heat-fluxes above the 0.25 MW/m^2 limit are typically a single spike due to noise, giving a strike-line width of the lower bound $\lesssim 1 \text{ cm}$. A problematic fit is shown in fig. 13 that will be discussed later.

On the vertical target, shown in fig. 6 the second structure at position 0.1 m is due to reflections, but as the the analysis is mostly concerned about the more narrow, higher peak, the reflection does not affect this analysis.

The fitted quantities were averaged by weighting with the power P_i of the data slice. Only slice i where fitting is attempted are included. The power-averaged quantity α is thus

$$\alpha = \frac{\sum_i \alpha_i P_i}{\sum_i P_i} \quad (1)$$

Fig. 7 shows on the left the connection length of some regions of the target regions. Regions of very long connection length $> 1000 \text{ m}$ indicate the location of the main strike line formed by the intersection of the island on the divertor target plates. It can be seen the main strike line is on the low iota target. Additionally, also on the vertical target long connection lengths are observed.

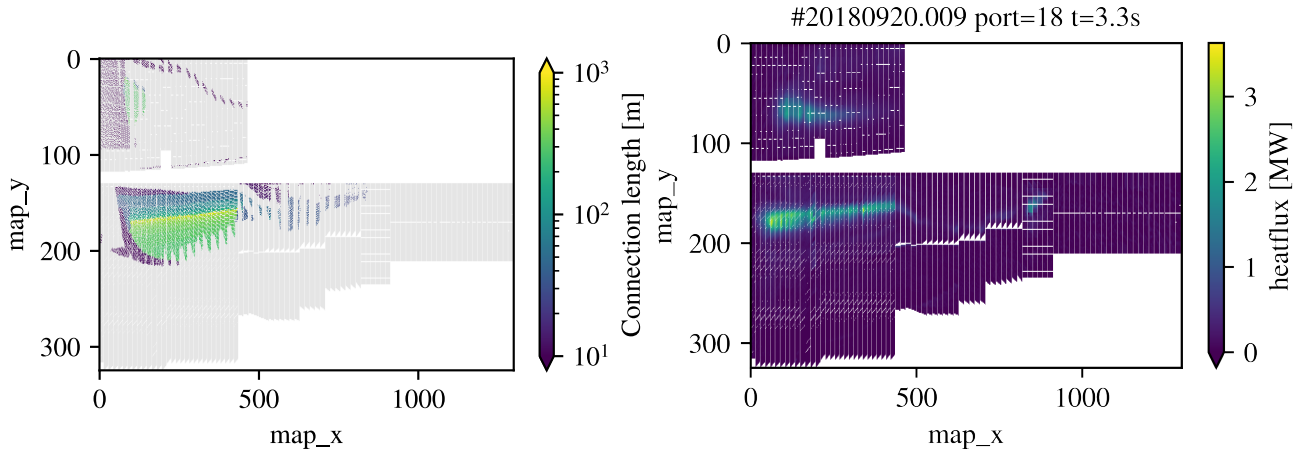


Figure 7. Shown on the left is a plot of the connection length mapped on to the target. Plotted in grey is the target regions where no traced field line ended. On the right is a plot of the heat-flux on the divertor at $t = t_1 + 3.3$ s for shot #20180920.009. The main strike line is on the left of the horizontal target, roughly in agreement with the long connection lengths. Additional heat loads on the high iota target as well as the vertical target are visible.

2.3. EMC3-EIRENE

EMC3-EIRENE is a Monte Carlo fluid transport and kinetic neutral code, that is capable of handling complex geometries, such as those commonly encountered in the SOL of stellarators. It has already been used in the past to model the edge of W7-X [16, 14, 15, 17, 18, 19, 20, 21]. While EMC3-EIRENE does capture some of the observations in experiments, especially global trends [14, 16], there is still disagreement in local parameters [30].

EMC3-EIRENE does include parallel transport in the form of advection as well as viscosity and parallel heat diffusivity. Perpendicular transport included in EMC3-EIRENE features anomalous diffusion based on some given particle and heat diffusion coefficients. EMC3-EIRENE does not require nested flux-surfaces and is only aware of the local magnetic geometry. For this reason the perpendicular diffusion is uniform in radial and bi-normal direction, i.e. $D \propto I - \vec{b}\vec{b}$ with \vec{b} the unit vector in the direction of the magnetic field and I the identity matrix. Drifts, like the $E \times B$ drift, are not included in EMC3-EIRENE. While EMC3-EIRENE is able to handle spatially varying perpendicular transport coefficients [15, 31], this feature is not used in the here presented study.

An analysis analogous to the one described in sec. 2.2 can be applied to simulated heat-flux data generated by EMC3-EIRENE. Thus, a direct comparison of experiment and modelling is performed. This allows to quantify the discrepancies and validate the modelling and the assumptions, for example the transport model, with experimental data.

In all cases the heat diffusion coefficient χ is set to $\chi = 3 \cdot D$, i.e. scaled with the diffusion coefficient. Note that the resulting heat transport is $q_{\perp} \propto n\chi$, i.e. has a density dependence even for constant χ .

2.4. xemc3

The majority of the analysis has been carried out using the xarray framework [32, 33]. For that the xemc3 [34] library has been implemented that reads the output of the EMC3-EIRENE routine into the xarray format. An extensive documentation, including documentation and online tutorials, is available online ‡.

3. Experimental data

For this analysis the W7-X experiments #20180920.009, #20180920.013 and #20180920.017 have been analysed. They are part of a density scan with an input power of 4.7 MW ECRH. They have been selected due to the low radiation fraction f_{rad} of around 0.15 . . . 0.35. Low f_{rad} avoids large effects of power dissipation in the volume. Thus transport is prominent and easier to study. The heat-flux on the divertor measured by IR was 3 . . . 4 MW, shown in fig. 8, with the time-averaged power per target between 330 kW and 496 kW. The peaks in the time evolution, shown in fig. 8, are due to CH₄ puffs and fuelling. The magnetic configuration used was the standard configuration. The toroidal plasma current increased over time and reached ≈ 5 kA after around 6 seconds towards the end of the discharge, with the exception of #20180920.017, where the maximal bootstrap current was around 2.5 kA. The SOL of W7-X is sensitive to plasma currents and the toroidal plasma current impacts the heat deposition [35, 36, 21]. For the here analysed discharges, the strike-line width is not significantly impacted by the toroidal current, but the strike-line position is a function of plasma current [29], as shown in fig. 8.

The line integrated density was $4 \cdot 10^{19} \text{ m}^{-2}$ to $8 \cdot 10^{19} \text{ m}^{-2}$. These low to medium density cases were selected as they feature a low radiative fraction. This allows to focus on the heat transport effect on the target heat load distribution, reducing the additional impact of radiation, simplifying the required physics to model the dynamics and reducing the system complexity as P_{rad} is a strong function of the electron temperature T_e . As the heat-flux is proportional to the density

‡ <https://xemc3.readthedocs.io/>

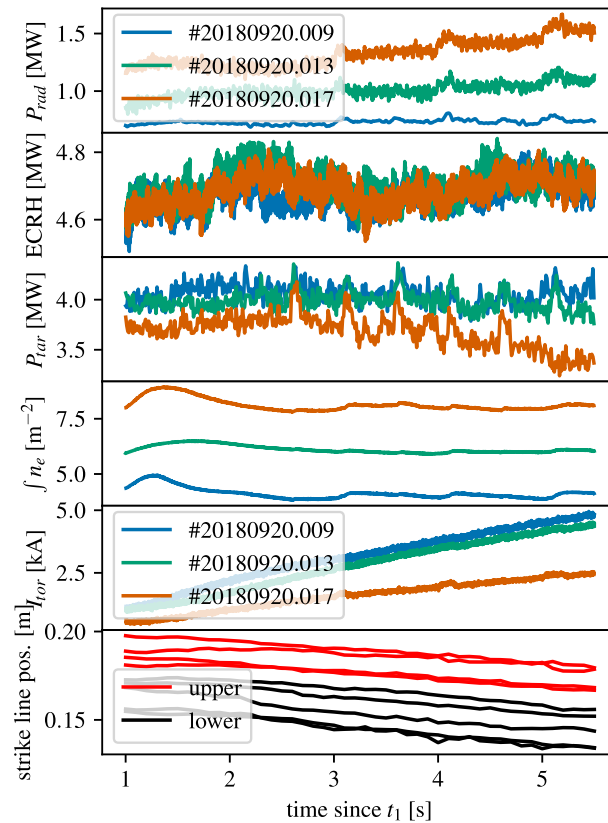


Figure 8. Overview of the time evolution of the radiated power P_{rad} , the ECRH heating power, the power on the target measured by IR, the line integrated density $\int n_e$, the toroidal plasma current I_{tor} and the strike line position from #20180920.009 on finger 24. For the target modules where no IR data was available, the average from the other targets was used to extrapolate to the total target power.

$q_{\perp} \propto n\chi$, a density scan was chosen for this study. The simulations do not feature the same densities, as in the simulations the separatrix density was set, while in the experiment the separatrix density is not well known. On the other hand the line integrated density is not known in the simulations, as the core region is not modelled.

Fig. 7 (right) shows an example of the spatial distribution of the target heat-flux in the projection described in fig. 3. Only the strike line on the low iota target is expected from simple field line tracing. The load on the vertical target can be explained by field line tracing in the reverse direction, while other loads are only possible due to cross-field transport.

3.1. Toroidal distribution

Fig. 9 shows a plot of the toroidal distribution of the heat-flux, by showing the mean power on the respective fingers, as introduced in fig. 2 and fig. 3.

No strong variation for the different half modules is observed, only half-module 28 shows an increased heat-flux at $\phi \approx -5^{\circ}$ on the horizontal target, as well as on the vertical target. For the lower divertors, most variation is observed at $\phi \approx -15^{\circ}$ where module 59 shows an increased heat load and module 49 shows a decreased heat load. These variations might be explained by field errors [26]. The calibration of the absolute values of the IR diagnostic was incomplete in OP 1.2b. This limits the reliability of comparisons between the different IR cameras and thus between the different half modules. The simulations assume stellarator symmetry and therefore only one half-module is modelled. They are inherently up-down symmetric and no variation between different modules is included. For these reasons the following analysis will focus on averages of the different modules.

Fig. 10 shows the experimental power per finger that was measured in the steady state part of a density scan for the upper divertors (top) and the lower divertors (middle). In general, a decreasing trend of power on the target with increasing density is observed, which is expected in the experiments as with increasing density the radiation increases, and thus the target heat load is reduced. An exception to the decreasing trend is the load at $\phi \approx 12^{\circ}$. The increased heat flux at this shadowed area is in agreement with an increased cross field transport with increasing density. Consequently the load on the middle of the horizontal target is increased, at least on the upper divertors. At low densities the main heat load on the horizontal target is mainly at $\phi \approx -15^{\circ}$ and less pronounced at $\phi \approx -5^{\circ}$. With increasing density the ratio of power at $\phi \approx -15^{\circ}$ over the power at $\phi \approx -5^{\circ}$ is reduced, suggesting an increased transport channel or a decrease in the losses from the transport channel to $\phi \approx -15^{\circ}$. Especially on the upper divertors, this results in an increased heat-flux at $\phi \approx -5^{\circ}$. At the same time

#20180920.009

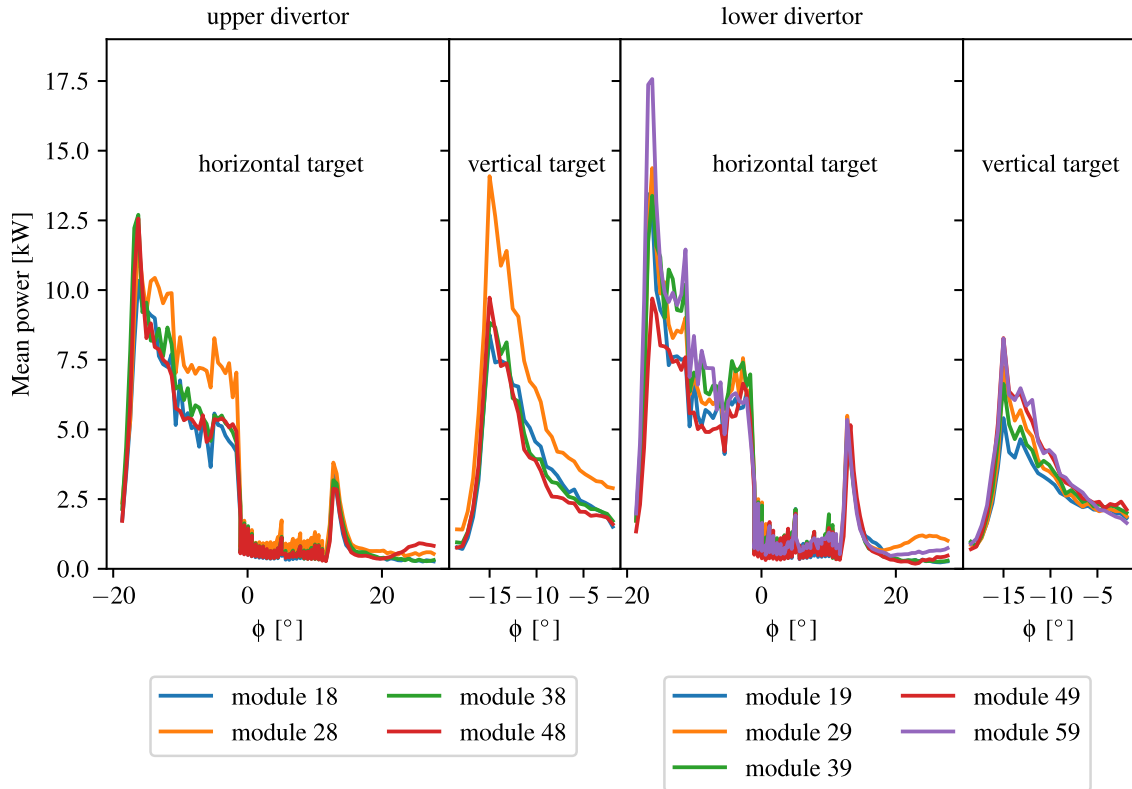


Figure 9. Plot of the time averaged power per finger for the steady-state phase of #20180920.009. The error bars denote the standard deviation of the time evolution. The fingers are introduced in fig. 2 and fig. 3. Note that the alternating structure in the middle of the horizontal target is caused by the numbering, even numbers are close to the pumping gap, while the odd numbers are further away. The different half modules are shown separately. No data from half-module 58 is available.

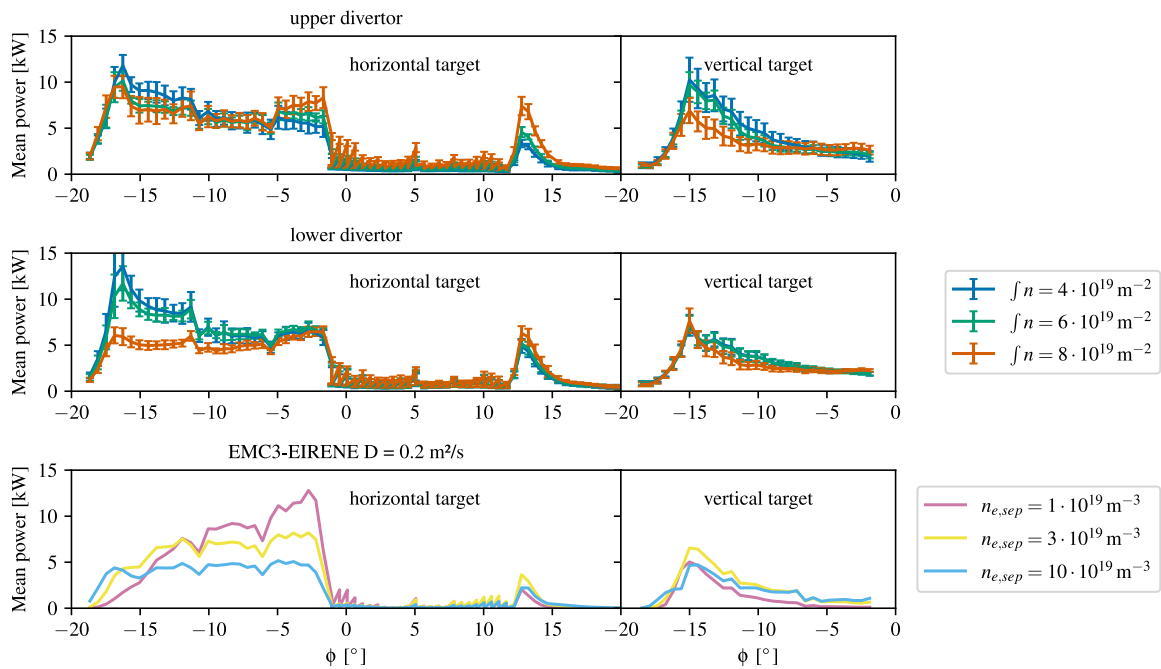


Figure 10. Plot of the time and module averaged power per finger for the steady-state phase of #20180920.009, #20180920.013 and #20180920.017 on top for the upper divertors and in the middle for the lower divertors. On the bottom are results from EMC3-EIRENE simulations with $D = 0.2 \text{ m}^2/\text{s}$ discussed in sec. 4. The error bars denote the standard deviation of the time evolution and inter module variation. As the simulations don't have a time component, only the experimental data has error bars. The P_{rad} for the simulations was 1 MW and for the experiments 0.68 MW to 1.7 MW, see fig. 8. The power on the divertor was 329 kW, 306 kW and 254 kW for the $n_{e,sep} = 1 \cdot 10^{19} \text{ m}^{-3}$, $n_{e,sep} = 3 \cdot 10^{19} \text{ m}^{-3}$ and $n_{e,sep} = 10 \cdot 10^{19} \text{ m}^{-3}$ case respective. Note that simulations and experiments do not match in density, as for the experiments the separatrix density is not well known, and for the simulations, due to the lack of core profiles, the line integrated density is not known.

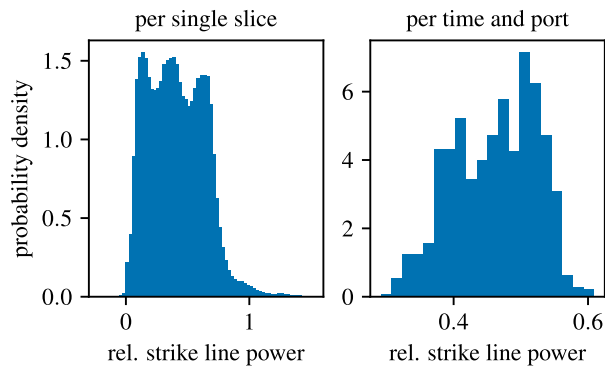


Figure 11. Distribution of the power in the main strike line compared to total power. On the left is the histogram for each single fitted slice, while on the right is the average for each divertor at each time. The shown data is for experiments #20180920.009 and #20180920.013.

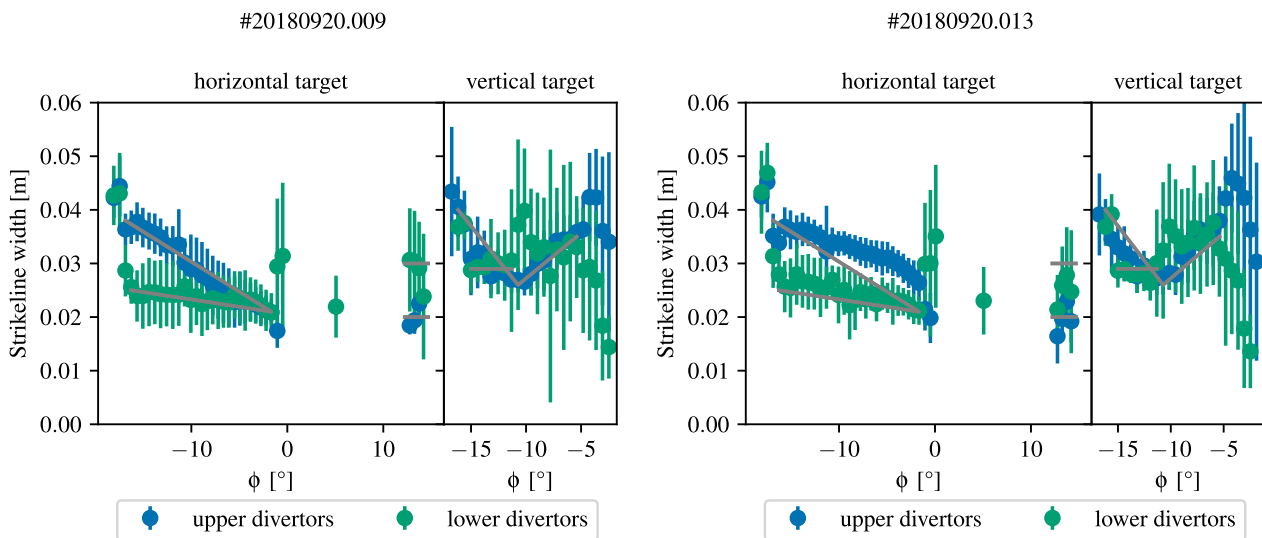


Figure 12. Plot of the time and module strike-line width per finger for the steady-state phase of #20180920.009 (left) and #20180920.013 (right). The points denote the power-averaged strike-line width for all fits, and the error-bars denote the power-averaged standard deviation. Shown is the narrow strike-line, that has been identified by fitting. Only finger with at least 2 kW average power are shown. The grey lines show estimates for #20180920.009 for upper and lower divertors, that will later be used for comparison to simulations. The large variation in the lower target on the vertical target is due to significant variation in the time traces for some of the fingers.

the heat-flux at $\phi \approx -15^\circ$ decreases. Note that, as can be seen on fig. 7, the target $\phi \approx -15^\circ$ ($\text{map_x} < 100$) is shadowed while at $\phi \approx -5^\circ$ ($\text{map_x} \approx 400$) is directly connected. As such this is in contrast to the expected behaviour.

Simulations with $D = 0.2 \text{ m}^2/\text{s}$, shown in the bottom plot in fig. 10, do not see the same trends with density. Here the peak of the mean power appears at $\phi \approx -5^\circ$ at low density, while $\phi \approx -15^\circ$ generally sees lower power. As the separatrix density is increased, the mean power at the $\phi \approx -5^\circ$ decreases, while the power at $\phi \approx -15^\circ$ increases slightly.

3.2. Strike-line

For the data shown in fig. 10 the strike-line has been analysed using the method discussed in sec. 2.2. Each module and time-slice has been analysed separately, to not broaden the strike line by averaging strike-lines at different positions due to the strike-line movement during the plasma discharge and e.g. camera misalignment and field errors [26] for different half modules.

The narrow feature identified is expected to be due to parallel plasma flow to the target. It is not yet clear what is causing the broad feature.

By integrating over the Gauss of the narrow feature, the power of the main strike line can be calculated. Fig. 11 shows the power observed in the narrow feature compared to the total observed power. Roughly 50% of the power on the divertor is in the main strike line. For the left figure, “per single slice” - values below 0 and above 1 are observed. This is due to bad fits, which can be caused by single points of high heat flux, that are fitted by a broader Gaussian. However, they are not frequent, and as such it is expected that they do not have a significant impact. The distribution for the averaged power on the right is not showing this behaviour, verifying that this indeed only outliers that show this behaviour.

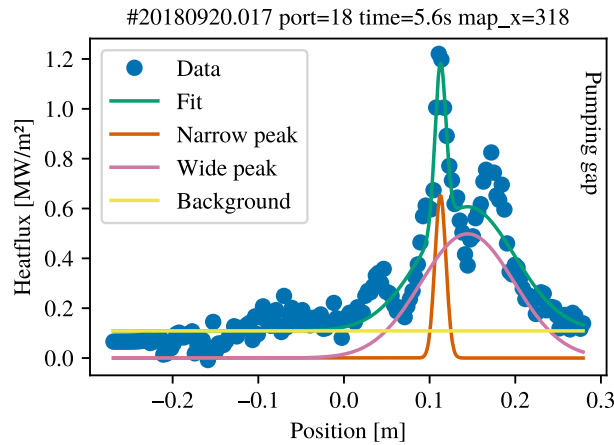


Figure 13. Plot of the IR data for the low iota target and $\text{map}_x=325$. Similar to fig. 5 but for like #20180920.017 instead of #20180920.009. Smaller structures in the fit prevent the expected convergence of the fit, and the fitted narrow peak is actually a smaller perturbation of the true main peak.

Fig. 12 shows the power-average (see (1)) of the width of the fitted narrow peak (see fig. 5) for the low and medium density cases #20180920.009 and #20180920.013. It can be seen that the strike-line width is in the range of 2 cm to 4 cm.

Both density cases show a similar behaviour in their strike-line width pattern on the upper and lower divertor target plates. Starting from $\phi \approx -20^\circ$, both the upper and lower divertor targets see comparable strike line widths and heat flux magnitudes. For the remainder of $\phi \approx 0^\circ$, on the lower divertor a narrow strike line is measured for the region of the high heat-flux, that stays constant, where the power flux is reduced, while on the upper target the strike-line is broader at $\phi \approx -15^\circ$, end gets more narrow towards the $\phi \approx -5^\circ$.

The strike-line width on the vertical target is comparable on the upper and lower divertors, at least for the points with significant power flux. The vertical targets of the upper and lower divertors mainly differ in their magnitude of the heat flux, as shown in fig. 10. The strike-line width at $\phi \approx 15^\circ$ is slightly wider on the lower divertor, however they are still the same within the standard deviation.

For the highest density case #20180920.017 (not shown), the average strike line widths across the divertor target could not be computed. Small-scale structures in the strike-line pattern keep the fits from converging reliably, with an example shown in fig. 13. The cause of these structures is not yet known. The small scale structures seem to be fixed in space, while the main strike line moves in time. As such it seems unlikely that the heat-flux of the plasma onto the target does contain such small-scale structures. It is currently hypothesized that these structures are caused by artefacts in the IR diagnostic. For example surface layers could modulate the radiation. Future work includes understanding the origin of these structures as well as extending the current fitting mechanism to be more tolerant of these modulations, such that reliable results of the strike line features can still be obtained even with their presence.

Fig. 14 shows the poloidal position of the strike-line for a part of the horizontal target. The lower divertors tend to have the strike line located somewhat closer to the pumping gap as compared with the upper divertors.

3.3. MPM data

For the above studied discharges no MPM data is available. Thus MPM data from #20181010.008, #20181010.016, #20181010.021 and #20181010.022 is used instead. The discharges used similar input power, same magnetic configuration and also feature low radiation fraction.

4. Simulations

The scrape-off layer of W7-X has been modelled using EMC3-EIRENE. For this the upstream density was scanned. The simulation relies on the stellarator symmetry of W7-X, and therefore only one half-module is modelled. Ideal coils are used and thus no error field effects are included. Drifts are not included as they are not yet implemented in the code.

The input heating power within the simulation domain of one half-module was set to be 470 kW, leading to a total of 4.7 MW for the whole device. The power was distributed evenly between ions and electrons, and enters the domain at the core boundary. The observed power on the divertor is up to 352 kW - giving a total power of ≈ 3.5 MW on all divertors. The upstream density was set to be fixed $n_{e,\text{sep}} = 1 \dots 10 \cdot 10^{19} \text{ m}^{-3}$. The cases $n_{e,\text{sep}} = 1 \cdot 10^{19} \text{ m}^{-3}$ and $n_{e,\text{sep}} = 3 \cdot 10^{19} \text{ m}^{-3}$ are roughly in the range of the experiments, while $n_{e,\text{sep}} = 10 \cdot 10^{19} \text{ m}^{-3}$ is a purely hypothetical case, as for such high densities the radiation fraction would be much higher. No pumping and fuelling is included in the simulations, and therefore particle balance is achieved via scaling the recycling flux to the amount needed for the fixed upstream density value. The radiation was fixed to 1 MW, achieved via carbon impurity radiation, giving a radiation fraction $\approx 21\%$. While in the experiment

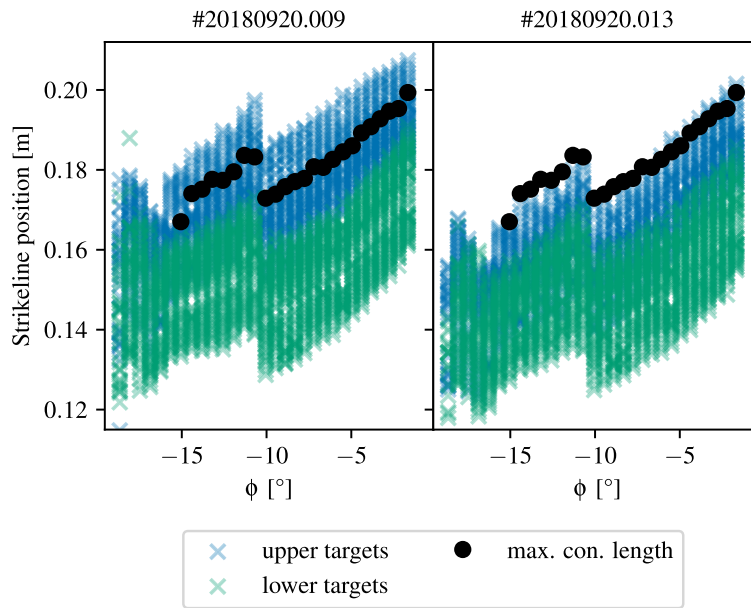


Figure 14. Poloidal position of the strike-line for some slices on the horizontal target, time averaged between 1 and 2 seconds. The different divertors are colour-coded based on the vertical position of the divertor, i.e. upper versus lower divertor. Note that the strike line position is not plotted as a function of time, but rather as a function of toroidal angle. Thus the jump around $\phi \approx -10^\circ$ is due to the definition of the local coordinate system. Also shown is the position of the long connection length from fig. 7 (left). Note that a deviation of the observed strike line from the position of the long connection length is expected due to the finite toroidal current.

the radiation fraction varies from 0.15 to 0.35, this was done to study the density and diffusion coefficient rather than the influence of the radiation fraction, which was recently studied by Feng et al. [16]. In particular the low f_{rad} was selected to avoid a dominant effect of the radiation.

The same magnetic field configuration was used in simulation as in experiment: the standard magnetic field configuration. A scan in density and diffusion coefficient was performed. EMC3-EIRENE stores where and how many particles leave the plasma domain. These particles can then be mapped onto the target surfaces in a post-processing step. In a next step the data has been mapped to the representation introduced in fig. 3. From this step on the same analysis, described in sec. 2.2, has been used for the simulated data as for the experimental data.

Fig. 15 shows plots of the electron density and temperature distribution of a simulation, where the diffusion coefficient was set to $D = 0.2 \text{ m}^2/\text{s}$ and the upstream density was set to $n_{e,sep} = 1 \cdot 10^{19} \text{ m}^{-3}$. The density shows a peak just in front of the target, at toroidal angle $\phi = 0$ at the upper and lower target plates. At the triangular shape ($\phi = \pi/5 = 36^\circ$) no target plates are present and thus also the density is not strongly peaked in the SOL. The temperature drops towards the target. While in this case the electron temperature at the separatrix is around 160 eV, the separatrix electron temperature is in all cases below 200 eV. Experimentally, separatrix electron temperatures were generally between 30 and 100 eV.

Similar to the experimental result, shown in fig. 7 (right), the main heat-flux is on the low iota target, with a strike line width and location similar to the experimental one. The main difference is that the main power is at $\phi \approx -5^\circ$, while in the experimental figure the main heat-flux is at $\phi \approx -15^\circ$.

4.1. Toroidal distribution

The toroidal distribution of the heat-flux, and how the change of the diffusion parameter impacts it is shown in fig. 16.

4.2. Strike-line

Besides the question where the power is deposited, the width of the strike line is of interest, as that influences over what area the heat is distributed, and thus also the peak heat-flux that the divertor has to withstand. Besides this more practical question, the strike line width gives also insight into the transport. Fig. 17 shows the fitted strike line width for a separatrix density $n_{e,sep} = 1 \cdot 10^{19} \text{ m}^{-3}$ with a diffusion coefficient scan in the range $D = 0.1 \dots 0.5 \text{ m}^2/\text{s}$. As mentioned, χ is scaled as $3D$. The strike line width for the other two density cases of interest $n_{e,sep} = 3 \cdot 10^{19} \text{ m}^{-3}$ and $n_{e,sep} = 10 \cdot 10^{19} \text{ m}^{-3}$ are shown in fig. 18. The experimentally observed density are likely between $n_{e,sep} = 1 \cdot 10^{19} \text{ m}^{-3}$ and $n_{e,sep} = 3 \cdot 10^{19} \text{ m}^{-3}$, as will be later discussed based on MPM data in sec. 4.3.

For the smallest $D = 0.1 \text{ m}^2/\text{s}$ the strike line width is $1 \dots 2 \text{ cm}$ on the low iota target, and thus smaller than the experimentally observed ones, shown before in fig. 12. For $D = 0.2 \text{ m}^2/\text{s}$ the strike line width is $2 \dots 3 \text{ cm}$ matching most closely to the experiment, while for $D = 0.5 \text{ m}^2/\text{s}$ the strike line width is in the range of $2 \dots 5 \text{ cm}$ and thus a bit larger than experimentally observed.

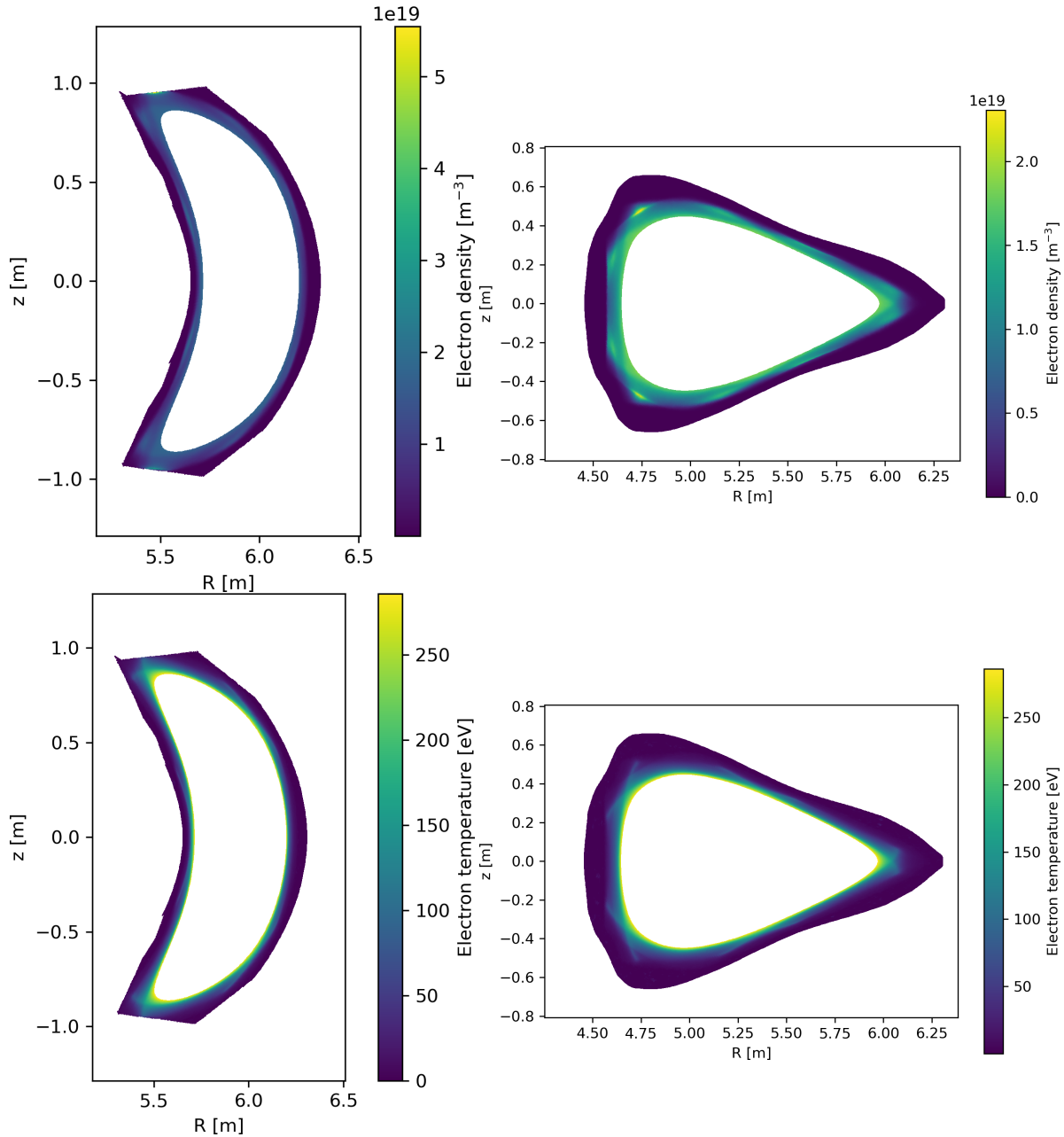


Figure 15. Density (top) and electron temperature (bottom) profiles for the $n_{e,\text{sep}} = 1 \cdot 10^{19} \text{ m}^{-3}$ case with $D = 0.2 \text{ m}^2/\text{s}$ at the bean shape, at $\phi = 0$ (left) and the triangular shape, at $\phi = \pi/5 = 36^\circ$ (right).

The peak at $\phi \approx 10^\circ$ agrees with experiment for the two larger diffusion coefficients. $D = 0.2 \text{ m}^2/\text{s}$ matches most closely for the lower divertors. A good match for the upper divertors is $D = 0.5 \text{ m}^2/\text{s}$ as well as the $D = 0.2 \text{ m}^2/\text{s}$ for the $n_{e,\text{sep}} = 3 \cdot 10^{19} \text{ m}^{-3}$ case.

4.3. Upstream data

To further compare the output of the models to experimental data, upstream data is beneficial as it is separated from the location that was optimised for. As introduced, the MPM can measure the density and temperature in the SOL, outside of the separatrix. Due to the separation from the targets, this can further ensure a matching transport model is chosen.

Figure 19 shows the density and temperature of a line of sight measured by the MPM diagnostic. Although no experimental MPM data is available for program #20180920.009, #20180920.013 and #20180920.017, similar programs with MPM data exist and are used as an upstream comparison to simulation. These programs have similar heating power, the same magnetic configuration and line integrated densities are in the range $4 \dots 6 \cdot 10^{19} \text{ m}^{-2}$. The simulation results, are plotted as lines in fig. 19. The simulations matching best the strike line width are plotted as lines, smaller D distributions are dotted and larger ones are dashed.

All simulations show essentially monotonic behaviour in the temperature and the density. This is in contrast to the experimental data. The experimental density shows for some cases a peak around the O-point, while for other cases it is monotonic. The temperature profile shows a clearly monotonic trend in the shadowed region, in contrast to the data in the

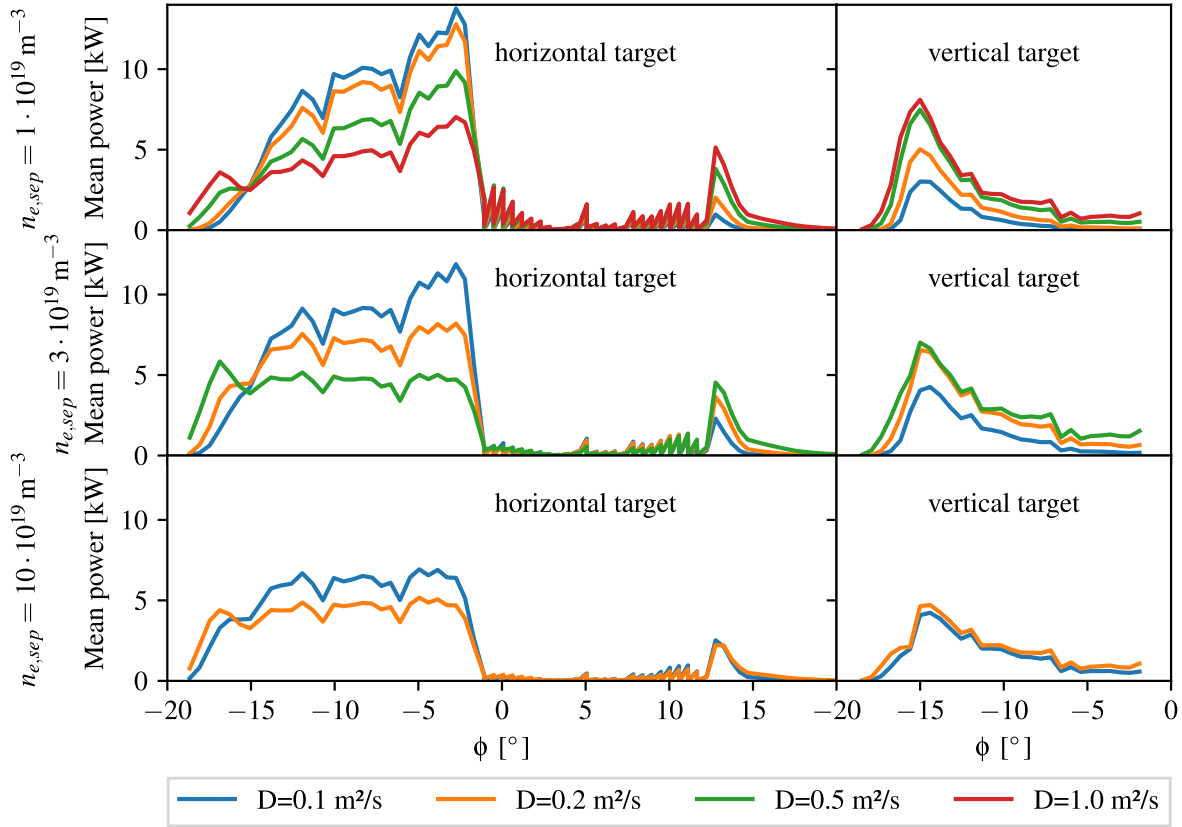


Figure 16. Plot of the power per finger for simulations with different separatrix density and different diffusion coefficient. This plot extends the density scan in fig. 10 with a scan of the diffusion coefficient D , with the heat diffusivity $\chi = 3D$ and $q_{\perp} \propto n\chi$.

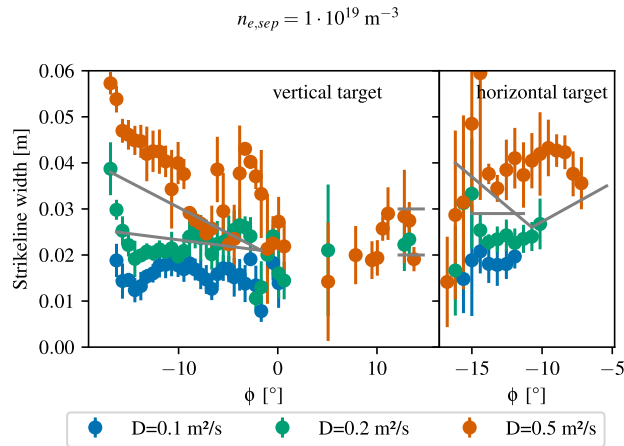


Figure 17. Mean of the strike-line width for the different fingers, as introduced in fig. 3. Note that the error bars are expected to be smaller than in the experimental data, shown in fig. 12, as the experimental data includes variations in time and across the different modules. Like fig. 12 only fingers receiving at least 1 kW of power are included. Simulation results for diffusion values $D = 0.1 \dots 0.5 \text{ m}^2/\text{s}$ and $n_{e,sep} = 1 \cdot 10^{19} \text{ m}^{-3}$. The grey lines show the estimates for the low density case from fig. 12.

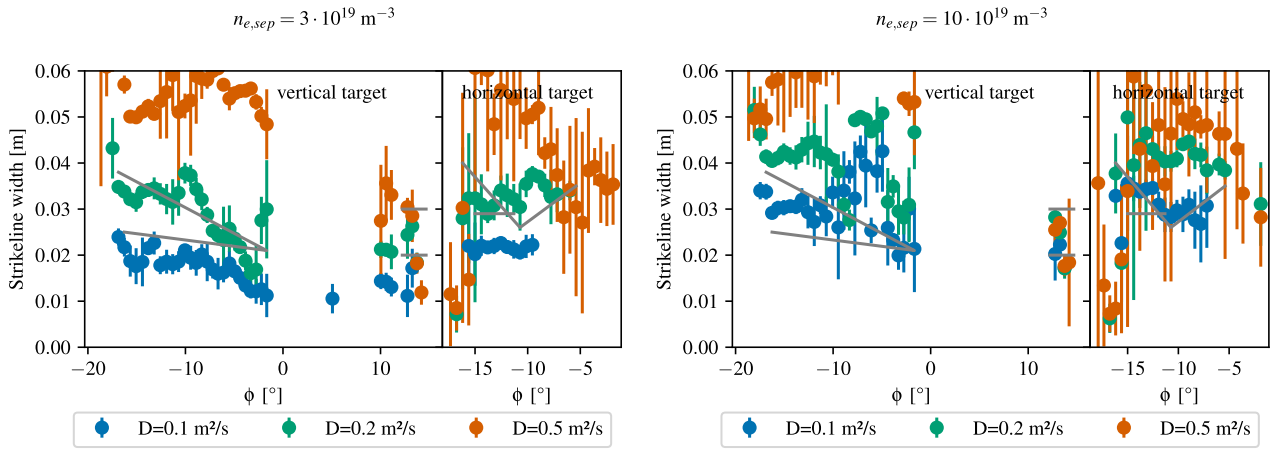


Figure 18. Mean of the strike-line width as a function of the fingers. Like fig. 17 but for $n_{e,sep} = 3 \cdot 10^{19} \text{ m}^{-3}$ and $n_{e,sep} = 10 \cdot 10^{19} \text{ m}^{-3}$.

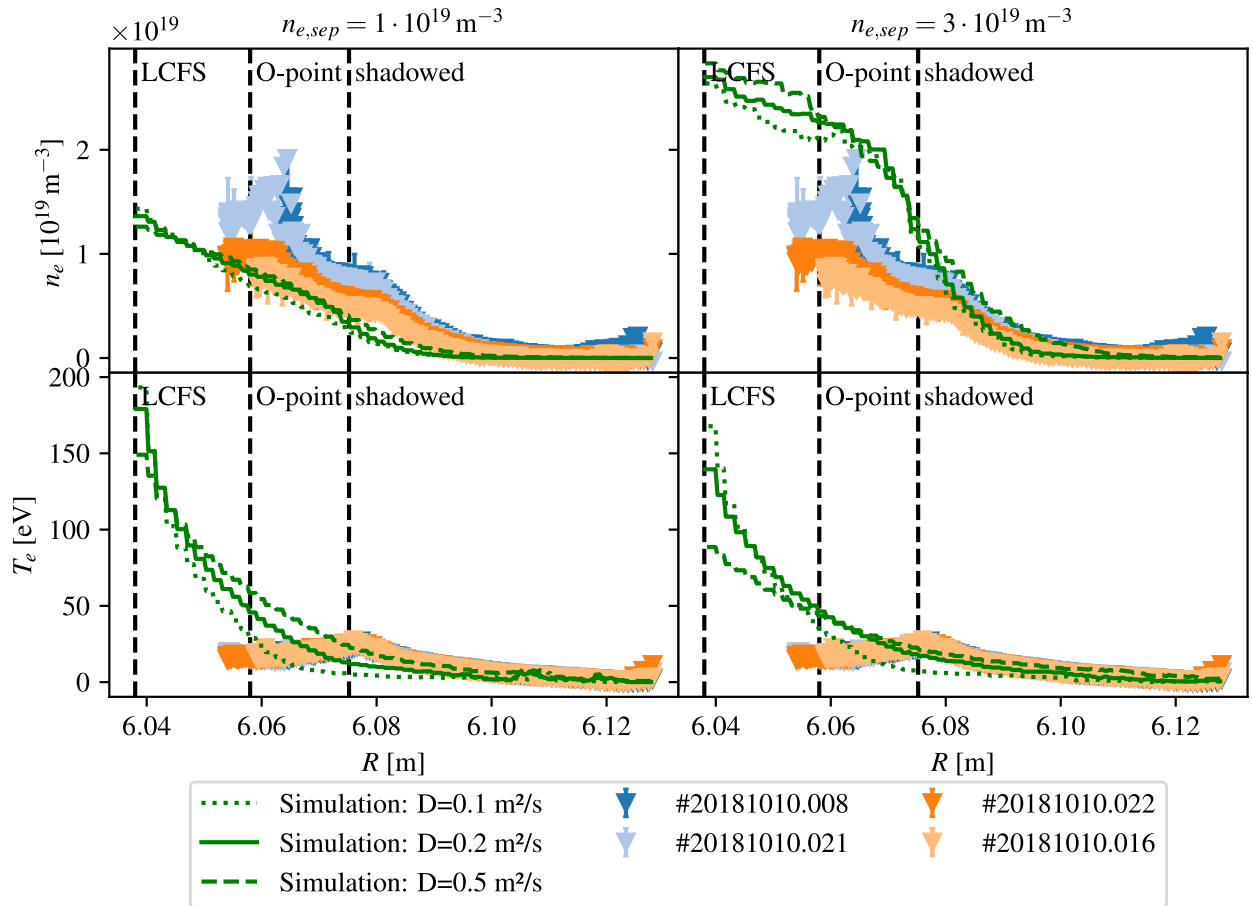


Figure 19. Plot of electron density and temperature as a function of the radial position. Shown is a 1D cut along the path of the MPM diagnostic [25, 24]. The experimental data from the MPM diagnostic is shown as symbols. The lines are the simulations with $n_{e,sep} = 1 \cdot 10^{19} \text{ m}^{-3}$ (left) and $n_{e,sep} = 3 \cdot 10^{19} \text{ m}^{-3}$ (right). Data from the $D = 0.1 \text{ m}^2/\text{s}$ is plotted as green dotted, $D = 0.2 \text{ m}^2/\text{s}$ as green line (best match based on strike line width) and $D = 0.5 \text{ m}^2/\text{s}$ as green dashed. The point magnetically closest to the O-point, as well as the position of the last closed flux surface (LCFS) and the onset of the shadowed area featuring short connection lengths, are also plotted.

longer connection length, where a hollow temperature profile is observed, featuring a reduction towards the O-point. The hollow temperature is observed in none of the simulations. In the shadowed region a roughly exponential behaviour for n_e and T_e is observed.

The separatrix density is an input parameter for the simulations. As such we can freely choose a density, to best match the experimental results. For all diffusion cases, the best match is between $n_{e,sep} = 1 \cdot 10^{19} \text{ m}^{-3}$ and $n_{e,sep} = 3 \cdot 10^{19} \text{ m}^{-3}$. Quantifying which case matches best, or which density would match best, is not well defined as the profiles do not match. $n_{e,sep} = 3 \cdot 10^{19} \text{ m}^{-3}$ matches very well in the shadowed area, while, depending on the experimental measurement, the $n_{e,sep} = 1 \cdot 10^{19} \text{ m}^{-3}$ case matches around the O-point.

For the temperature, all simulations feature a to high temperature towards the island centre. The MPM was not able to measure closer to the separatrix, but the separatrix temperature is generally estimated to be below 100 eV. In general with increasing D the separatrix temperature decreases, and the temperature fall-off-length increases.

5. Discussion

The experimental heat-flux data from W7-X has been analysed determining the toroidal distribution as well as using fits of the strike line. The fits allowed to determine the position and the width of the strike line, with the exception of the higher density case #20180920.017 where the fit did not converge reliably, as smaller structures were present.

Determining the shape of the strike line allows to determine how much of the power is deposited on the main strike line versus how much in total is deposited on the divertor. A significant amount of power is observed by the IR cameras to be deposited outside of the main strike-line ($\sim 1 \text{ MW}$). This power is seen as a broad feature and its cause is not yet known. Surface layers, which have been observed to build up on certain areas of the divertor over the campaign [37], may increase the IR emissivity of the targets, thus possibly creating an artefact of higher heat flux. Another possible explanation is power load by plasma radiation close to the divertor. Initial calculation seem to agree with the radiation hypothesis, however an in-depth study is outside of the scope of this paper. Future work is planned to investigate this feature.

The strike line width from the experiments has been determined to be around 2 to 4 cm in the magnetic standard configuration. This is true for all areas on the target where a significant heat-flux is observed, including the low iota target. The 2 to 4 cm is observed independent of the connection length. This observation is reproduced in the simulations, where for a given density and diffusion the strike line width is roughly constant for all significantly loaded areas.

For the experimental data no clear trend of the strike line width with density is observed. For the simulations a clear trend of increasing strike line width with increasing density is observed. In the simulations the density variation was however much larger.

While it is possible to match the strike line width to the experimental ones, none of the simulations matched the toroidal distribution, especially at the low iota target.

6. Conclusion and Summary

For comparing experimental and simulation data of the target heat-fluxes, a fitting routine has been implemented, which works reliably for well-behaved IR heat-flux data. Future work will make the fitting more robust to counteract any possible artefacts in the heat-flux analysis.

In the past some qualitative comparison between experiments and simulations have been attempted for the SOL of W7-X. The here performed quantitative comparison shows that, in order to reproduce the experimentally observed strike line width of the range 2 to 4 cm, diffusion coefficients in the range of $0.2 \text{ m}^2/\text{s}$ are needed in the magnetic standard configuration for low to medium density cases.

There are significant differences between simulations and experiments, that could not be reproduced by the simulation. Some differences are expected to be due to a lack of drifts in EMC3-EIRENE: e.g. the up-down asymmetry on the divertor target plates. Additionally, small toroidal asymmetries are observed in experiment, which are expected due to the non-perfect error field correction. Due to the inherent symmetry of the simulation, they are, like drifts, not expected to be reproduced. However, other discrepancies remain which are not expected, such as the difference in the toroidal distribution of the heat flux on the low iota target. Additionally hollow temperature profiles in the islands are measured by the MPM diagnostic, which has not been reproduced by the simulations.

Non-isotropic transport coefficients could be used in EMC3-Eirene to match both upstream values as well as target heat-flux data.

7. Acknowledgement

This work has been carried out using the xarray framework [32, 33]. Some task have been parallellised using GNU parallel [38].

The simulation presented here are available [39]

- [1] KLINGER, T. et al., Nuclear Fusion **59** (2019) 112004.
- [2] KLINGER, T. et al., Plasma Physics and Controlled Fusion **59** (2017) 014018.
- [3] WOLF, R. et al., Nuclear Fusion **57** (2017) 102020.
- [4] SUNN PEDERSEN, T. et al., Physics of Plasmas **24** (2017) 055503.

- [5] BEIDLER, C. D. et al., *Nature* (2021).
- [6] PEDERSEN, T. S. et al., **61** (2018) 014035.
- [7] PEDERSEN, T. S. et al., **59** (2019) 096014.
- [8] HAMMOND, K. C. et al., **61** (2019) 125001.
- [9] FRERICHS, H. et al., *Review of Scientific Instruments* **87** (2016) 11D441.
- [10] KILLER, C. et al., **62** (2020) 085003.
- [11] KILLER, C. et al., **61** (2021) 096038.
- [12] ZOLETNIK, S. et al., *Plasma Physics and Controlled Fusion* **62** (2019) 014017.
- [13] LIU, S. et al., *Nuclear Fusion* **59** (2019) 066001.
- [14] WINTERS, V. R. et al., *Plasma Physics and Controlled Fusion* **63** (2021) 045016.
- [15] FENG, Y. et al., *Contributions to Plasma Physics* **54** (2014) 426.
- [16] FENG, Y. et al., *Nuclear Fusion* **61** (2021) 086012.
- [17] SCHMITZ, O. et al., *Nuclear Fusion* (2020).
- [18] WURDEN, G. et al., *Nuclear Fusion* **57** (2017) 056036.
- [19] SCHMID, K. et al., *Nuclear Materials and Energy* **25** (2020) 100821.
- [20] EFFENBERG, F. et al., *Nuclear Materials and Energy* **18** (2019) 262.
- [21] LORE, J. et al., *Nuclear Fusion* **59** (2019) 066041.
- [22] JAKUBOWSKI, M. et al., *Review of Scientific Instruments* **89** (2018) 10E116.
- [23] SIEGLIN, B. et al., *Review of Scientific Instruments* **86** (2015) 113502.
- [24] KILLER, C. et al., **59** (2019) 086013.
- [25] KILLER, C. et al., *Journal of Instrumentation* **17** (2022) P03018.
- [26] LAZERSON, S. A. et al., **60** (2018) 124002.
- [27] BYRD, R. H. et al., *Mathematical programming* **40** (1988) 247.
- [28] BRANCH, M. A. et al., *SIAM Journal on Scientific Computing* **21** (1999) 1.
- [29] GAO, Y. et al., *Nuclear Fusion* **59** (2019) 106015.
- [30] FENG, Y. et al., *Nuclear Fusion* **61** (2021) 106018.
- [31] ZHANG, W. et al., *Nuclear Fusion* **56** (2016) 036007.
- [32] HOYER, S. et al., *Journal of Open Research Software* **5** (2017).
- [33] HOYER, S. et al., <https://doi.org/10.5281/zenodo.4563695>, pydata/xarray: v0.17.0, 2021.
- [34] BOLD, D. et al., <https://doi.org/10.5281/zenodo.5562266>, dschwoerer/xemc3: v0.1.0, 2021.
- [35] GEIGER, J. et al., *Contributions to Plasma Physics* **50** (2010) 770.
- [36] GEIGER, J. et al., *Contributions to Plasma Physics* **51** (2011) 99.
- [37] MAYER, M. et al., *Physica Scripta* **T171** (2020) 014035.
- [38] TANGE, O., *GNU Parallel 2018*, Ole Tange, 2018.
- [39] BOLD, D. et al., <https://zenodo.org/record/5762079>, EMC3-EIRENE simulations of Wendelstein 7-X - diffusion coefficient and density scan, 2021.